



**International Journal of Bio-Inspired Computation**

ISSN online: 1758-0374 - ISSN print: 1758-0366

<https://www.inderscience.com/ijbic>

---

**Optimised context encoder-based fusion approach with deep learning and nonlinear least square method for pan-sharpening**

Preeti Singh, Sarvpal Singh, Marcin Paprzycki

**DOI:** [10.1504/IJBIC.2023.10060652](https://doi.org/10.1504/IJBIC.2023.10060652)

**Article History:**

Received:	21 March 2022
Last revised:	31 January 2023
Accepted:	31 August 2023
Published online:	22 January 2024

---

## Optimised context encoder-based fusion approach with deep learning and nonlinear least square method for pan-sharpening

---

Preeti Singh\*

Department of Computer Science and Engineering,  
Madan Mohan Malaviya University of Technology,  
Gorakhpur, UP, India  
Email: singh.preeti294@gmail.com  
\*Corresponding author

Sarvpal Singh

Department of Information Technology and Computer Application (ITCA),  
Madan Mohan Malaviya University of Technology,  
Gorakhpur, Gorakhpur, UP, India  
Email: spsingh@gmail.com

Marcin Paprzycki

Department of Computer Science,  
Polish Academy of Science, Poland  
Email: marcin.paprzycki@ibspan.waw.pl

**Abstract:** In this study, a hybrid optimisation strategy is used to build a deep learning system for pan sharpening. The final output image is examined using a weighted nonlinear regression model after the spatial resolution of the low resolution-hyperspectral image (LR-HIS) and high resolution multi-spectral image (HR-MSI) is increased. The deep maxout network (DMN), which used residual learning to acquire its priors, is given the HR-MSI. Moreover, DMN is trained by fractional competitive multi-verse feedback tree algorithm (FrCMVFTA). Finally, the output produced from DMN and a weighted nonlinear regression model is combined together for obtaining pan sharpened image. The PSNR value obtained by the FrCMVFTA-based DMN for the dataset Indian pines by varying the number of bands is 5.41% greater than the existing approaches. The DD value obtained by the FrCMVFTA-based DMN for the dataset Pavia by varying the number of bands is 31.47% greater than existing approaches.

**Keywords:** pan sharpening; deep maxout network; feedback artificial tree algorithm; degree of distortion; competitive multi-verse optimiser.

**Reference** to this paper should be made as follows: Singh, P., Singh, S. and Paprzycki, M. (2024) 'Optimised context encoder-based fusion approach with deep learning and nonlinear least square method for pan-sharpening', *Int. J. Bio-Inspired Computation*, Vol. 23, No. 1, pp.53–67.

**Biographical notes:** Preeti Singh did her BTech from ITM, Gorakhpur, Department of Computer Science & Engineering and MTech from Azad Institute of Engineering and Technology, Lucknow Department Computer Science and Engineering. She is currently pursuing her PhD from Madan Mohan Malaviya University of Technology, Gorakhpur. Her field of research include neural network, deep learning, remote sensing, and image processing.

Sarvpal Singh is a Professor and Head at Department of Information Technology and Computer Application (ITCA) in M.M.M. University of Technology, Gorakhpur. He did his BE in Computer Science from Marathwada University, Aurangabad and ME in Computer Science from Thapar Institute of Engineering and Technology, Patiala. He did his PhD from Deen Dayal Upadhyay Gorakhpur University. His field of research include wired/wireless networking, mobile and cloud computing and Linux OS.

Marcin Paprzycki is an Associate Professor at the Systems Research Institute, Polish Academy of Sciences. He has an MS from Adam Mickiewicz University in Poznan, Poland, a PhD from Southern Methodist University in Dallas, Texas, and a Doctor of Science from the Bulgarian Academy of Sciences. He is a senior member of IEEE, a senior member of ACM, a Senior

Fulbright Lecturer, and an IEEE CS Distinguished Visitor. He has contributed to more than 450 publications and was invited to the program committees of over 500 international conferences. He is on the editorial boards of 12 journals and a book series.

## 1 Introduction

In modern days, the application of remote sensing images is quickly developed, but an anticipated image with high spatial resolution and spatial resolution cannot be attained through current technologies (Aiazzi et al., 2016; Hou and Zhang, 2016; Bhanot, 2021). Due to the increasing application of high-resolution (HR) multi spectral (MS) imaging in various domains, including spectral unmixing, environmental monitoring, and water quality estimation (Simone et al., 2002), several pan-sharpening approaches have been developed. The pan-sharpening technique is employed for getting an HRMS image through the fusion of HR PAN (HRPAN) image as well as low resolution MS image (Yang et al., 2020). The pan sharpening process is employed to consider the entire advantages of available spectral and spatial information, and it is attained from low spatial resolution MSI, which is connected with high spatial resolution PAN image (Luo et al., 2020). Remote sensing images are extensively utilised in several domains, like military, academic regions, and civil, because of the fast development of satellite images. However, the described remote sensing techniques have an inherent trade-off between spectral resolution and spatial resolution. As a result, for a certain remote sensing sensor, acquired grey PAN images are frequently thought to have a greater resolution than MS images. Besides, the pan-sharpening tasks are frequently observed as an essential pre-processing process for several remote sensing data applications (Zhang et al., 2022b; Wu et al., 2020), including land cover classification (Lv et al., 2019), urban impervious surfaces (Shao et al., 2019) and change identification (Bovolo et al., 2009; Wang et al., 2021).

The technique of combining the relevant data from two or more images into one image is known as image fusion. A data cube called the high-resolution image (HS image) contains a number of 2-dimensional (2D) spectral channels. Each of these channels provides information on the brightness or reflectance of a scene over a specific, limited wavelength range. The huge number of spectral information with regards to physical characteristics of material substances has obtained effectual achievement for target detection (Lin et al., 2018; Zhang et al., 2002a; Zhou et al., 2019; Zheng et al., 2022), land use classification (Li et al., 2017), and denoising (Yuan et al., 2018; Xie et al., 2020). Furthermore, high PAN and HR images as well as low spatial resolution MS images, are afforded concurrently through remote sensing satellites, like WorldView-2, Gaofen-2, and IKONOS, which overlay similar land regions (Ma et al., 2020). The HR PAN images, along with one band, usually include well defined spatial information, while low resolution MS images with multiple spectral bands can define the spectral diversity. Hence, fusion

techniques, named pan-sharpening schemes, are developed for fusing images. In addition, the HR MS images encompass spectral as well as spatial characteristics (Luo et al., 2020).

Various researchers applied deep learning methods to the pan-sharpening process (Wang et al., 2019). In modern days, deep neural network (DNN) driven pan-sharpening methods are employed for the concept of spatial image resolution (Cai and Huang, 2020). Additionally, various researchers are devised convolution neural networks (CNN)-based deep learning methods for the pan-sharpening process, like PanNet (Yang et al., 2017a), progressive structure-conditional generative adversarial networks (PSGAN) (Qian et al., 2018), and probabilistic neural network (PNN) (Masi et al., 2016). Deep learning-driven pan sharpening techniques treat the original HR MS images as ground truth images (Ma et al., 2020). Generally, the pan sharpening approaches are categorised into several types, such as Bayesian methods, MR analysis (MRA), matrix factorisation schemes, component substitution (CS), and tensor-based techniques (Liu et al., 2018b). The gram schmidt (GS) and also adaptive GS (Aiazzi et al., 2007) are demonstrative of CS-based techniques (Xie et al., 2020) in which the common CS-based fusion model is considered for effectual execution of pan-sharpening methods, and it employs linear injection method rather than backward or complex forward transmissions. The major contribution of this paper is explicated as follows:

- FrCMVFTA-based DMN is developed for pan sharpening.
- FrCMVFTA is developed by incorporating FAT and CMVO technique along with FC and DMN is trained by designed by FrCMVFTA.

## 2 Literature survey

This section explains the benefits and drawbacks of the current pan sharpening methods. Yang et al. (2020) developed a detailed optimisation approach for pan-sharpening. This approach effectively handled spectral information, although computational complexity was decreased. Vivone et al. (2020) introduced robust regression technique for the Pan sharpening process. The appropriate balancing was performed between the computational problem and fusion performance. However, this technique failed to enhance the overall performance. Xie et al. (2020) introduced HS pan sharpening approach depending on 3-Dimensional (3-D) generative adversarial network (HPGAN). This approach effectively improves the spatial information as well as preserves spectral information. Even though this pan sharpening approach did not solve the

over fitting problems. Luo et al. (2020) presented an unsupervised convolutional neural network (CNN) for pan sharpening. This scheme enhanced the information reuse with the transmission but still failed to reduce the redundant data.

He et al. (2020) devised spectral fidelity CNN, named HSpE\_Nets for HS pan sharpening. The time consumption is highly reduced in this method, although it failed to solve various spectral distortions, like the edge of the structure in an enlarged box. Cai and Huang (2020) developed deep CNN (DCNN) for spatial resolution-guided progressive pan-sharpening process. This technique effectively improves the quantitative indicators, even though it failed to reduce the execution time. Ma et al. (2020) presented a pan-sharpening process that depends on generative adversarial network (GAN), termed as Pan-GAN. The information loss was highly decreased, but still, this scheme failed to improve spectral information protection. Wang et al. (2021) introduced dual path fusion network (DPFN) for the pan sharpening process. This method effectively reduces spectral and spatial distortion. However, this scheme failed to decrease the calculation complexity owing to the high amount of matrix operations.

### 3 Problem formulation

The high resolution-hyper spectral image (HR-HSI), as well as HR multi-spectral image (HR-MSI) are specified as matrices (Dian et al., 2019). Moreover, matrices are defined with two dimensions in which the first dimension represents the number of spectral bands, whereas other dimension signifies the number of pixels. The obtained LR-HSI is denoted as  $E \in \kappa^{M \times m}$  where  $M$  indicates the number of spectral bands, and  $m = B / o$  here,  $B$  implies the number of pixels as well as  $o$  symbolises decimation factor in LR-HSI. Besides, HR-MSI is illustrated as,  $D \in \kappa^{t \times B}$  where  $t$  signifies spectral band quantity. Thus, the fused image  $D_{Hin}$  is expressed as,

$$D_{Hin} = KD \quad (1)$$

where  $K$  refers to spectral basis, and  $D$  denotes equivalent coefficients. The LR-HIS  $T$  is spatially down sampled to  $F$ , which is given by,

$$E = KDRM \quad (2)$$

where  $R \in \kappa^{B \times B}$  implies convolution between HR-HSI bands as well as the function of point spread of the sensor. The term  $R$  represents blur matrix. Furthermore, columns of spatial down-sampling matrix indicate the identity matrix subset.

The HR-MSI  $F$  is spectrally down sampled to  $D$ , and it is illustrated as,

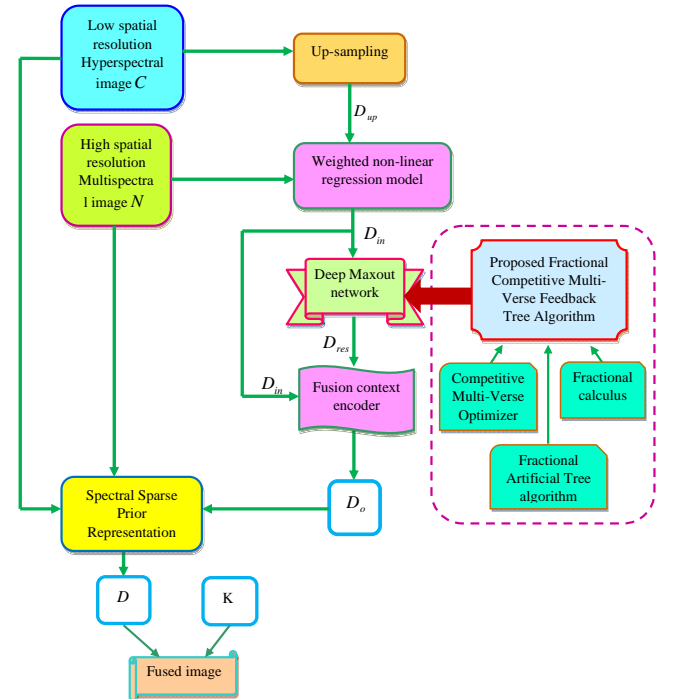
$$F = HKD \quad (3)$$

where  $H$  denotes spectral down sampling matrix in which rows are engaged with spectral information's of the multispectral sensor.

### 4 Developed Deep maxout spectral sparse prior representation with context encoder for pan-sharpening

The block diagram of the pan sharpening model based on devised FrCMVFATA-based DMN is demonstrated in Figure 1. The hybrid optimisation driven DMN for the pan sharpening process is introduced. The pan-sharpening process is employed for fusing multi-spectral image and panchromatic images. Moreover, various approaches are developed using pan-sharpening, although these methods do not afford standardised implementation. Therefore, an effective pan sharpening approach is designed using a hybrid optimisation-based deep learning technique. Here, the LR-HSI and HR-MSI are subjected to up-sampling approach (Kwon and Tai, 2015) in which spatial resolution LR-HSI is increased as well as the final output image is passed to a weighted nonlinear regression model. The weighted nonlinear regression approach utilises the outcome image obtained from the upsampling process. The HR-MSI is given to DMN (Sun et al., 2018), which learned the priors by means of residual learning. Moreover, DMN is trained by designed FrCMVFATA, and it is newly introduced by integrating FAT (Li et al., 2020) and CMVO (Benmessahel et al., 2020) techniques along with FC (Bhaladhare and Jinwala, 2014). Finally, the output produced from DMN and a weighted nonlinear regression model is combined together to obtain the pan-sharpened image.

**Figure 1** Block diagram of pan-sharpening model based on developed FrCMVFATA-based DMN (see online version for colours)



Let us consider, LR-HSI image database as  $C$  with  $h$  quantity of LR-HSI images, which is specified as,

$$C = \{V_1, V_2, \dots, V_v, \dots, V_h\} \quad (4)$$

where  $V_v$  denotes  $v^{\text{th}}$  LR-HSI image and  $h$  represents the whole number of images.

Additionally, let us consider HR-MSI image data as  $N$  with  $d$  number of images, which is illustrated as,

$$N = \{G_1, G_2, \dots, G_e, \dots, G_d\} \quad (5)$$

where  $G_e$  refers  $e^{\text{th}}$  HR-MSI image, and  $d$  is total HR-MSI images.

#### 4.1 Up sampling

The LR-HSI images are specified as  $C$ , which are fed to up-sampling process for up-sampling the images into essential resolution. The importance of utilising up-sampling method (Kwon and Tai, 2015) is in order to decrease the image blurriness and also reducing the noises present in an image through recollecting natural image structure. Furthermore, up-sampling process increases the spatial information's of HSI with the management of HR red green blue (RGB) image.

The fast learning driven single image super resolution approach is applied for upsampling  $C$ , formulating structures of HR in  $U$  and also spectrum correlation between several wavelength channels in  $C$ . The image patches are sampled based on the instances of training in which every patch is in the dimension of  $5 \times 5$  with primitive structures of  $W$ ,  $C$  and  $U$  expressed as  $MW$ ,  $MC$  and  $MU$ . Besides, ratio of resolution among  $W$  and  $C$  in training instances is 2. The up-sampling of the target  $R$  is performed several times, if up-sampling factor is bigger than 2. The spectrum substitution is modified following to every spatial up-sampling and the process is continued until  $C$  meets the target resolution. With consideration of every sampled patch, the luminance  $B$  is estimated with its RGB values, after that mean subtraction is employed to build a feature vector through pixel stacking of  $B$  channel image. The sample patch clustering is performed into  $J$  groups. Moreover, these clustered patches are considered as exemplars for super resolution.

Let us assume  $K = \{KW(g, c), KC(g, c), KU(g, c)\}$ , such that  $1 \leq g \leq J$ , and  $1 \leq c \leq N(g)$ , which expresses the trained exemplars, where  $J$  indicates count of clustered group and  $N(g)$  specifies exemplars count in every set. The exemplars of every set pose similar primitive structures, and consequently, exemplar in every set is referred as linear combination of other exemplars in the similar set, which is

$$K(g, c) = \sum_{o=1, o \neq c}^{N(g)} \varphi_j K(g, j)$$

here  $\varphi_j$  implies linear coefficients. Therefore, linear coefficients are estimated depends on  $MC$  and  $MU$ , which is minimised as,

$$\varphi^* = \arg \min_{\varphi} \left\| \begin{bmatrix} \sigma_C \\ \sigma_U \end{bmatrix} - \sum_{j=1}^{N(g)} \varphi_j \begin{bmatrix} K_C(g, j) \\ K_U(g, j) \end{bmatrix} \right\|_2^2 \quad (6)$$

Moreover, optimal solution  $\varphi^*$  is formulated by means of simple linear regression. With the consideration of  $\varphi^*$ ,  $\sigma_w$  is reconstructed as,

$$\sigma_w = \sum_{j=1}^{N(g)} \varphi_j^* K_w(g, j) \quad (7)$$

After the computation of  $\sigma_w$ , patch means of  $C$  is estimated in order to get an accurate upsampled  $W$ . The reconstructed patches are accurate since overlapping patch regions enhanced the local compatibility. The structure is added for guiding total variation regularisation because the input  $C$  is noisy.

$$W^o = \arg \min_W \|W - \hat{W}\|_2^2 + \eta (1 - |\nabla_o U|) |\nabla_w|_1 \quad (8)$$

where  $W$  denotes solution after exemplar super-resolution,  $\nabla_o U$  implies maximal absolute gradient of  $U$  transverse RGB channels,  $|\nabla_w|_1$  refers to total variation regularisation, and  $\eta$  symbolises regularisation weight with rate 0.01.

#### 4.2 Weighted nonlinear regression model

Let us consider HR image  $N$  and also upsampled image  $D_{up}$  (He et al., 2007) for performing the pan sharpening process.

$$H(v, N) = \frac{1}{2} (w - P(v)N)^X (w - P(v)N) + \frac{\beta}{2} N^X X(\tau)N \quad (9)$$

where  $v$  indicates unknown motion vector,  $\beta$  specifies regularisation parameter,  $w$  is matrix vector form, which is expressed as  $w = P(v)N + l$ , here the term  $l$  is given by,

$$l = [l_1^X, \dots, l_Z^X]^X \quad (10)$$

The matrix  $P(v)$  is formed by nonlinear, differentiable functions of an unknown motion parametric vector.  $l = [l_1^X, \dots, l_Z^X]^X$  is the vector representing the discrete, concatenated and lexicographically ordered  $l_k$ . Therefore, the weighted nonlinear regression model integrates both up-sampled and HR-MSI images.

#### 4.3 Construction of residual image using developed fractional competitive multi-verse feedback artificial tree algorithm-based deep maxout network

This section explains the hybrid optimisation-based DMN that was developed for generating the residual image.

##### 4.3.1 Deep maxout network

The outcome of the weighted nonlinear regression approach  $D_{in}$  is considered as input for DMN. The DMN (Sun et al., 2018) model indicates the multiple layer maxout, which utilises various benefits of trainable activation function approximator as well as non-saturated activation function. The activation function is taken into consideration by DMN,

which substantially speeds up training and is used for constructing pan-sharpening. As an example of how hidden elements can be activated,

$$Q_{q,a}^1 = \max_{e \in [1, j_1]} S^H \rho_{qa} + T_{qa} \quad (11)$$

$$Q_{q,a}^2 = \max_{e \in [1, j_2]} S_{q,a}^1 \rho_{qa} + T_{qa} \quad (12)$$

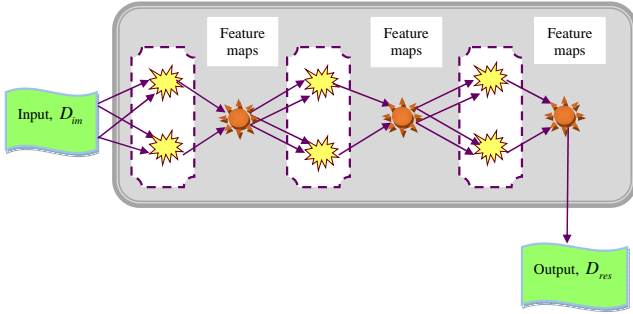
$$Q_{q,a}^o = \max_{e \in [1, j_l]} Y_{q,a}^{j-1H} \rho_{qa} + T_{qa} \quad (13)$$

$$Q_{qa}^j = \max_{e \in [1, j_j]} Q_{q,a}^{j-1H} \rho_{qa} + T_{qa} \quad (14)$$

$$Z_q = \max_{e \in [1, j_j]} Q_{q,a}^j \quad (15)$$

where  $l$  implies total layers in DMN,  $j_l$  signifies the number of units in the  $l^{\text{th}}$  layer,  $\rho_{qa}$  refers to weights and  $T$  indicates bias. Moreover, DMN activation is stronger for approximating the arbitrary permanent activation function. The output produced from DMN is the residual image, which is signified as  $D_{res}$ . The structural representation of DMN is shown in Figure 2.

**Figure 2** Architecture of DMN (see online version for colours)



#### 4.3.2 Developed fractional competitive multi-verse feedback artificial tree algorithm for the training process of deep maxout network

Based on an FrCMVFATA that was developed to boost performance, DMN goes through its training procedure. In light of this, FAT (Li et al., 2020) and CMVO (Benmessahel et al., 2020) approaches, in addition to FC (Bhaladhare and Jinwala, 2014), are used to introduce the developed FrCMVFATA. The movement of biological material and revised branch theories encourage the use of the FAT approach. Many other types of real-world optimisation problems could be resolved using this approach. In addition, the competitive strategy between universes serves as the inspiration for the CMVO method. For resolving challenges with global optimisation, the CMVO is effective. The fundamental objective of this method is to create pair-wise competition, which will increase the rate of exploration in the search domain. By utilising winner-based learning, this methodology greatly improves the ability to exploit. However, FC is coupled with CMVO and FAT techniques to reduce processing time

and information loss and to boost computing performance. The developed FrCMVFATA's algorithmic procedure is described as follows:

- 1 Initialise the population of the branch

In the process of receiving feedback, the branch is first initialised. A random sample of branches is selected from the branch population when the feedback process begins, and it is produced by the transfer of organic matter, which is defined as,

$$A_{new} = \text{randchoose}(A, b) \quad (16)$$

where  $A$  represents branch population,  $A_{new}$  refers to a selected population of the branch, and  $b$  implies the ratio of newly selected branch to branch population. Here,  $A_{new} \in \rho_{qa}, T$ .

- 2 Error computation

The error function, which is viewed as a minimisation problem, is used to identify the best solution. The best solution is one that produces the least mean square error (MSE). By, the MSE is calculated.

$$\gamma = \frac{1}{z} \sum_{\omega=1}^z (v_z - D_{res})^2 \quad (17)$$

where  $z$  denotes the total number of samples,  $\gamma$  symbolises MSE,  $v_z$  indicates expected output, and  $D_{res}$  is obtained output from DMN.  $\omega$  represents the training sample range i.e.,  $1 < \omega < z$ .

- 3 Determine self-propagating operator

The self-propagating operator is carried out in order to renew the branch depending on CMVFATA, which is given by,

$$A_{new} = \frac{k_2 + k_3}{k_2 + k_3 + 1 - \text{rand}(0,1) \times i} \left[ \frac{k_1 \times Z + k_2 \times A_a + k_3 \times A}{k_2 + k_3} (1 - \text{rand}(0,1) \times i) + \text{rand}(0,1) \times A_{best} \times i \right] \quad (18)$$

To apply FC, substitute  $A_z$  on both sides,

$$A_{new} - A_z = \frac{k_2 + k_3}{k_2 + k_3 + 1 - \text{rand}(0,1) \times i} \left[ \frac{k_1 \times Z + k_2 \times A_a + k_3 \times A}{k_2 + k_3} (1 - \text{rand}(0,1) \times i) + \text{rand}(0,1) \times A_{best} \times i \right] - A_z \quad (19)$$

The FC concept is included in above expression,

$$D^f [A_{new}] = \frac{k_2 + k_3}{k_2 + k_3 + 1 - rand(0,1) \times i} \left[ \frac{k_1 \times Z + k_2 \times A_a + k_3 \times A}{k_2 + k_3} (1 - rand(0,1) \times i) + rand(0,1) \times A_{best} \times i \right] - A_z \quad (20)$$

$$A_{new} - fA_z - \frac{1}{2}fA_{z-1} - \frac{1}{6}(1-f)A_{z-2} - \frac{1}{24}f(1-f)(2-f)A_{z-3} = \frac{k_2 + k_3}{k_2 + k_3 + 1 - rand(0,1) \times i} \quad (21)$$

$$\left[ \frac{k_1 \times Z + k_2 \times A_a + k_3 \times A}{k_2 + k_3} (1 - rand(0,1) \times i) + rand(0,1) \times A_{best} \times i \right] - A_z$$

$$A_{new} = A_z(f-1) + \frac{1}{2}fA_{z-1} + \frac{1}{6}(1-f)A_{z-2} + \frac{1}{24}f(1-f)(2-f)A_{z-3} + \frac{k_2 + k_3}{k_2 + k_3 + 1 - rand(0,1) \times i} \quad (22)$$

$$\left[ \frac{k_1 \times Z + k_2 \times A_a + k_3 \times A}{k_2 + k_3} (1 - rand(0,1) \times i) + rand(0,1) \times A_{best} \times i \right]$$

where  $k_1$ ,  $k_2$  and  $k_3$  are random number ranges from  $[0, 1]$ ,  $i$  denotes constant,  $i = 0.382$ ,  $A_{best}$  is best branch position,  $A$  indicates mean location rate of relevant universes,  $A_a$  is winner universe in  $k^{\text{th}}$  round of competition,  $rand(0, 1)$  implies random integer among 0 and 1, and  $Z$  symbolises coefficient, and it is illustrated as,

$$Z = 1 - \left( \frac{y^{1/H}}{Y^{1/H}} \right) \quad (23)$$

where  $y$  is current iteration  $H = 6$ , and  $Y$  represents maximum iteration.

#### 4 Discover dispersive propagation operator

The dispersive propagation operator is finished to offer branch evolution once the self-propagation operator is finished. In this situation, a second branch is found based on both the new branch and the position of the original branch. The half territory is utilised to produce a new branch at random in this case. Consequently, the dispersive operator is defined as,

$$A_{qo} = A_{po} + rand(-1,1) \times Q_p \times i \quad (24)$$

$$A_{xo} = A_{po} + rand(0,1) \times A_{qo} \quad (25)$$

where  $A_{qo}$  and  $A_{xo}$  signifies  $o^{\text{th}}$  element of  $A_q$  and  $A_x$ . Here,  $A_q$  and  $A_x$  are generated two branch locations as well as  $Q_p$  indicates branch territory.

#### 5 Re-evaluation of error

Once the branch location updation is finished, then the error of every branch is estimated using equation (17).

#### 6 Termination

All the above steps are continued until the best optimal solution is obtained.

Algorithm 1 deliberates the pseudo-code of developed FrCMVFTA.

#### Algorithm 1 Pseudo code of devised FrCMVFTA

S. no.	Pseudo code of introduced FrCMVFTA
1	<b>Input:</b> Arbitrary branch location $A$ , iteration $y$ , and maximum iteration $Y$
2	<b>Output:</b> Optimal branch position $A_{best}$
3	Start
4	Initialise branch population and other algorithmic parameters
5	Estimate the initial population
6	$Cycle = 1$
7	Repeat
8	Estimate the count of branches in branch population $A$
9	if $A \geq \alpha$ where, $\alpha$ is number of branches in branch population
10	if $Cycle > 1$
11	Incorporate current and previous branch population
12	Consider $\alpha$ better branches between new set of branches
13	<b>end if</b>
14	<b>for</b> $o = 1$ to $a$
15	<b>for</b> $p = 1$ to $\alpha$
16	<b>for</b> $z = 1$ to $\sigma$ do
17	<b>If</b> territory of branch $p$ is not crowd
18	Execute crossover operator to create new branch
19	<b>else</b>
20	Accomplish self-evolution operator for new branch based on equation (22)
21	<b>end if</b>
22	<b>If</b> new branch is higher than branch $p$
23	Break present for loop
24	<b>end if</b>
25	<b>end for</b>
26	<b>If</b> better branch is not found
27	Perform random operator for generating new branch
28	<b>end if</b>
29	Update the branch with new branch
30	<b>end for</b>
31	Obtain new branch

```

32 Update the best solution
33 end for
34 Select initial branch population for feedback
35 else
36 for  $p = 1$  to  $A$ 
37 for  $z = 1$  to  $\sigma$  do
38 If territory of branch  $p$  is not crowd
39 Perform dispersive propagation operator for the new
branch
40 else
41 Perform self-evolution operator for new branch using
equation (22)
42 end if
43           If a new branch is superior than branch  $p$ 
44 Break present for loop
45 end if
46 end for
47           If better branch is not found
48 Execute random operator to create a new branch
49 end if
50 Update the branch with the new branch
51 end for
52 Attain new branch
53 Update the optimal solution
54 Integrate current and previous branch population
55     end if
56      $Cycle = cycle + 1$ 
57     Until the function evaluation number reaches the
maximal function evaluation number
58     Return  $A_{best}$ 
59 end

```

#### 4.4 Content encoder-based fusion of images

Here, output produced from DMN  $D_{res}$  is combined with the output of the weighted nonlinear regression model  $D_{in}$  based on the content encoder model. The output of DMN and weighted nonlinear regression technique is considered as input for encoder and it generates latent feature representation. Finally, the fused image  $D_{Fin}$  is obtained by fusing both outputs from DMN and the weighted nonlinear regression method.

##### 4.4.1 Encoder decoder pipeline

The encoder and decoder are linked based on the channel wise fully connected layer. This process permits every unit in the decoder to reason about total image content (Dian et al., 2018).

###### 1 Encoder

The Alexnet architecture serves as the foundation for the encoder in this case. The first five convolutional layers in this scenario, followed by a pooling layer,

were used to estimate the representation of the dimensional features. The convolution layers connect to every feature map, even if they never directly link every point in a given feature map. Information cannot be transferred directly from one corner of the feature map to another if the encoder model only comprises convolution layers. In this way, activations are connected directly to one another and fully interconnected inner products handle information handling. The characteristics of the encoder are also connected to the decoder via a channel-wise fully linked layer.

###### 2 Channel wise fully connected layer

This layer is more important for propagating information in activations of every feature map. Although, it is having no parameters linking to various feature maps as well as propagates the information in the feature map.

###### 3 Decoder

Based on encoder features, the decoder approach generates the image's pixels. Additionally, a channel-wise entirely connected layer links the characteristics of the encoder and the decoder. After the channel-wise fully connected layer, five up convolution layers with learned filters and the rectified linear unit (ReLU) activation function are added.

#### 4.4.2 Loss function

Moreover, the employed context encoders are trained through retreating the ground truth content of input images. Although, there are various similarly probable behaviours in order to fusing the images, and it is dependable with context. Decoupled joint loss function is used in this procedure to manage the output's multiple modes and context continuity. Reconstruction loss, on the other hand, may be trusted to accurately represent the model of image fusion and maintain consistency with its contexts. The masks are automatically generated for image and training iterations during the training process. The loss function is expressed as,

$$L_{joint} = \tau_{rec} L_{rec} + \tau_{adv} + L_{adv} \quad (26)$$

where  $L_{rec}$  depicts reconstruction loss, and  $L_{adv}$  represents an adversarial loss.

The reconstruction loss is specified as,

$$L_{rec}(n) = \left\| \hat{C} \circ (n - R((1 - \hat{C}) \circ n)) \right\|_2 \quad (27)$$

where  $\circ$  refers element wise product operation,  $\hat{C}$  implies binary mask,  $R$  signifies context encoder, and  $n$  represents ground truth image. The adversarial loss is mainly depending on generative adversarial network (GAN), which is illustrated as,

$$L_{adv} = \max_X \mathfrak{R}_{n \in N} \left[ \log X(n) + \log \left( 1 - X \left( R(1 - \hat{C}) \circ n \right) \right) \right] \quad (28)$$

where  $X$  is the adversarial discriminator.

## 5 Optimising fusion problem using developed Deep maxout-context encoder based spectral sparse prior representation

The major intent is to formulate the fused image  $D_{Fin}$  in which the term  $D$  must be estimated (Dian et al., 2018), which is expressed as.

The HR-HSI is employed in order to solve the optimisation problem, which is given by,

$$\min_D \|I - D_{Fin} RM\| + \|F - ZKD\| + \chi_2 \|D_{Fin} - D_o\| \quad (29)$$

Hence,  $D_o$  is included in order to solve the sparsity and the resultant expression is denoted as,

$$\min_F \|I - D_{Fin} RM\| + \|F - YKD\| + \chi_1 |D| + \chi_2 \|D_{Fin} - D_o\| \quad (30)$$

where  $\chi_2$  specifies regularisation attribute. Let us consider  $P_1 = D$  and  $P_2 = KD$ , as well as produces augmented Lagrangian function, which is specified as,

$$\begin{aligned} E(D, P_1, P_2, O_1, O_2) = & \|F - P_2 RM\|^2 + \|F - YKD\| \\ & + \chi_1 \|P_1\| + \chi_2 \|KD - D_o\| \\ & + v \left\| P_1 - D + \frac{P_1}{2v} \right\|^2 \\ & + v \left\| P_2 - KD + \frac{P_2}{2v} \right\|^2 \end{aligned} \quad (31)$$

where  $P_1$  and  $P_2$  indicates the Lagrangian multiplier. Through decreasing augmented Lagrangian function outcomes,

$$D^{h+1} = \arg \min_F (E, P_1^h, P_2^h, O_1^h, O_2^h) \quad (32)$$

$$P_2^{h+1} = \arg \min_{P_2} E(D^{h+1}, P_1^h, P_2, O_1^h, O_2^h) \quad (33)$$

$$P_1^{h+1} = \arg \min_{P_1} E(D^{h+1}, P_1, P_2^{h+1}, O_1^h, O_2^h) \quad (34)$$

The sub-problems of expression (32) (33) and (34), which are given below as,

$$\begin{aligned} D^{h+1} = & \left[ (YK)^O YK + (\chi_2 + v) K^O K + vX \right]^{-1} \\ & \left[ (YK)^O F + \chi_2 K^O D_o + v \left( P_1^h + \frac{O_1^r}{2v} \right) \right] \\ & \left[ +vK^O \left( P_2^h + \frac{O_2^h}{2v} \right) \right] \end{aligned} \quad (35)$$

$$P_2^{h+1} = \left[ I(RM)^O + v \left( KD^{h+1} - \frac{P_2^h}{2v} \right) \right] \left[ RM(RM)^O + vX \right]^{-1} \quad (36)$$

$$P_1^{h+1} = \max \left( \text{soft} \left( D^{h+1} - \frac{O_1^r}{2v}, \frac{\chi_1}{2v} \right), 0 \right) \quad (37)$$

$$O_1^{h+1} = O_1^h + 2v(P_1^{h+1} - D^{h+1}) \quad (38)$$

$$O_2^{h+1} = O_2^h + 2v(P_2^{h+1} - KD^{h+1}) \quad (39)$$

where

$$\text{soft}(D, A) = \text{sign}(D) * \max(|D| - A, 0),$$

and  $\max(D, A)$  indicates the maximum of  $D$  and  $A$ .

## 6 Results and discussion

This section discusses the results and analyses of the developed FrCMVFITA-based DMN for pan-sharpening. This section includes contains details on the experimental setup, dataset description, experimental results, comparative methodologies, analysis, and commentary.

### 6.1 Experimental setup

The newly developed FrCMVFITA-based DMN for pan-sharpening is performed using the PYTHON tool, which is run on a computer running Windows 10OS, an Intel i3 processor, and 8GB of RAM.

### 6.2 Dataset description

The implementation of the developed pan sharpening approach is carried out by means of two datasets, including Indian Pines, Pavia (Indian Pines and Pavia Centre and University data, 2022).

#### a Indian Pines

This data is collected using an AVIRIS sensor considering the Indian Pines test site in North-western Indiana. It includes 145 pixels with 224 spectral reflectance bands considering wavelength, which ranges from 0.4 to  $2.5 \times 10^{-6}$  metres. This data contains one-third forest and two-thirds agriculture.

#### b Pavia

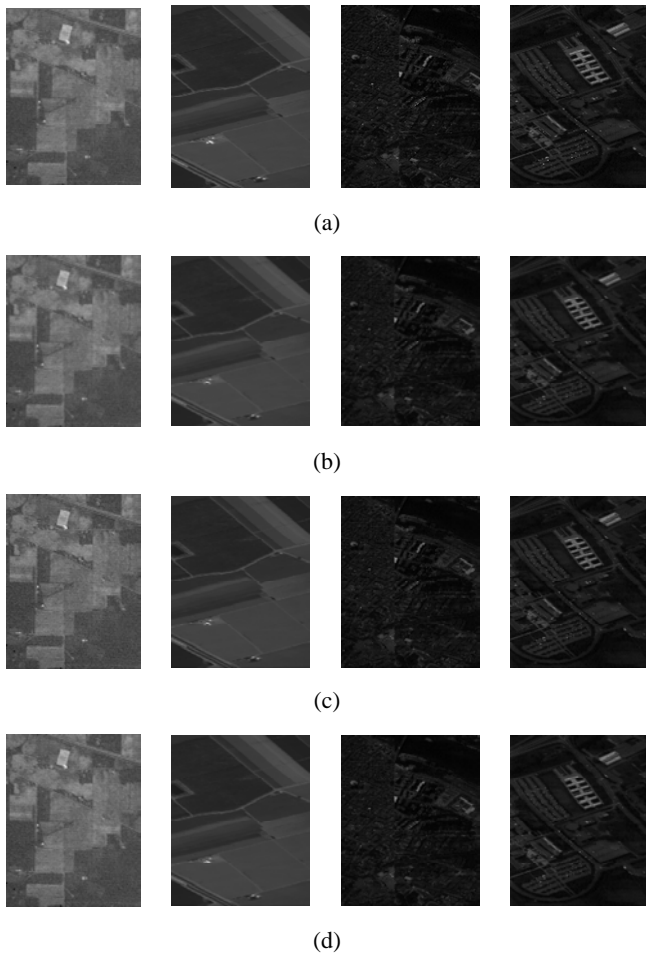
This data is accomplished with ROSIS sensor through flight operation throughout Pavia. In this dataset, Pavia includes 102 spectral bands and 1096\*1096 pixels images. Furthermore, the geometric resolution of the Pavia database is 1.3 metres.

### 6.3 Experimental results

The experimental pan-sharpening results are shown in Figure 3. Figure 3(b) shows the outcomes of the spectral

sparse prior, while Figure 3(a) shows the input images 1, 2, 3, and 4. The output from the weighted nonlinear regression approach is also shown in Figure 3(c), and the fused end result image is shown in Figure 3(d).

**Figure 3** Experimental results of developed FrCMVFTA-based DMN, (a) input image-1, 2, 3 and 4 (b) output image-1 for input image-1,2,3 and 4 (c) output image-2 for input image-1, 2, 3 and 4 (d) final fused image-1 for input image-1, 2, 3 and 4



#### 6.4 Comparative techniques

The existing pan-sharpening techniques, namely Context based GLP (Yang et al., 2020), CNN (Vivone et al., 2020), low rank fuzzy fusion (Luo et al., 2020), HOGAN (Ma et al., 2020), CMVFTA-based DMN, pose and expression robust spatial-aware GAN (PSGAN) (Liu et al., 2018a), and path aggregation network (PanNet) (Yang et al., 2017b) are considered for evaluating the performance of developed FrCMVFTA-based DMN model.

#### 6.5 Comparative analysis

The developed FrCMVFTA-based DMN approach is compared in this section using two datasets, including Indian Pines, and Pavia along with the number of bands and neta value.

##### 6.5.1 Comparative analysis using Indian pines

This section describes the examination of the FrCMVFTA-based DMN developed using Indian Pines data by varying the number of bands and neta value.

###### 1 Analysis by changing the number of bands

Figure 4 displays the examination of the created FrCMVFTA-based DMN for performance indicators with various band counts. The examination of the newly introduced FrCMVFTA-based DMN for Peak signal-to-noise ratio (PSNR) is presented in Figure 4(a). In 20 bands, the developed FrCMVFTA-based DMN's PSNR is 51.655 dB, compared to 26.667 dB for context-based GLP, 10.453 dB for CNN, 18.892 dB for low rank fuzzy fusion, 42.952 dB for HOGAN, 46.959 dB for PanNet, 47.898 dB for PSGAN, and 48.856 dB for CMVFTA-based DMN. Figure 4(b) shows the examination of the developed FrCMVFTA-based DMN for DD. In 40 bands, the developed FrCMVFTA-based DMN's DD is 0.064 dB, while the context-based GLP's DD is 0.097 dB, CNN's DD is 0.189 dB, the low rank fuzzy fusion DD is 0.410 dB, the HOGAN DD is 0.070 dB, the PanNet DD is 0.066 dB, the PSGAN DD is 0.077, and CMVFTA-based DMN is 0.064 dB. The examination of the newly developed FrCMVFTA-based DMN for SSIM is presented in Figure 4(c). Context based GLP is 0.714 dB, CNN is 0.844 dB, Low rank fuzzy fusion is 0.741 dB, HOGAN is 0.781 dB, PanNet is 0.871 dB, PSGAN is 0.889 dB, and CMVFTA-based DMN is 0.906 dB. The developed FrCMVFTA-based DMN's SSIM is 0.924 dB in 20 bands. The examination of the newly introduced FrCMVFTA-based DMN for CC is presented in Figure 4(d). In 20 bands, the created FrCMVFTA-based DMN's CC is 0.832 dB, context based GLP's is 0.552 dB, CNN's is 0.697 dB, low rank fuzzy fusion's is 0.860 dB, HOGAN's is 0.752 dB, PanNet's is 0.785 dB, PSGAN's is 0.760, and the CMVFTA-based DMN is 0.793 dB.

###### 2 Analysis by shifting neta value

Figure 5 depicts the comparison of the created FrCMVFTA-based DMN after changing the neta value with various parameters. The introduced FrCMVFTA-based DMN for PSNR analysis is plotted in Figure 5(a). When the neta value is 20, the created FrCMVFTA-based DMN's PSNR is 45.217 dB, Context based GLP's is 29.999 dB, CNN's is 13.179 dB, Low rank fuzzy fusion's is 22.043 dB, PanNet's is 42.657 dB, HOGAN's is 40.870 dB, PSGAN's is 41.279 dB, and the CMVFTA-based DMN is 43.084 dB. In Figure 5(b), the analysis of the created FrCMVFTA-based DMN for DD is shown. When neta is 40, the created FrCMVFTA-based DMN's DD is 0.074 dB, Context-based GLP's is 0.103 dB, CNN's is 0.169 dB, Low-rank Fuzzy Fusion's is 0.408 dB, HOGAN's is 0.080 dB, PanNet's is 0.076 dB, PSGAN's is 0.081, and the CMVFTA-based DMN is

0.102 dB. The new FrCMVFTA-based DMN for SSIM analysis is depicted in Figure 5(c). When neta is equal to 20, the created FrCMVFTA-based DMN's SSIM is 0.824 dB, while Context-based GLP is 0.547 dB, CNN is 0.690 dB, Low rank fuzzy fusion is 0.852 dB, HOGAN is 0.745 dB, PanNet is 0.778 dB, PSGAN is 0.752 dB, and CMVFTA-based DMN is 0.785 dB. The introduced FrCMVFTA-based DMN for CC is analysed and plotted in Figure 5(d). When neta is equal to 20, the CC of the developed FrCMVFTA-based DMN is 0.632 dB, Context based GLP is 0.825 dB, CNN is 0.857 dB, Low rank fuzzy fusion is 0.691 dB, HOGAN is 0.770 dB, PanNet is 0.786 dB, PSGAN is 0.801 dB, and CMVFTA-based DMN is 0.916 dB.

**Figure 4** Comparative analysis of developed FrCMVFTA-based DMN using Indian Pines with a number of bands, (a) PSNR (b) DD (c) SSIM (d) CC (see online version for colours)

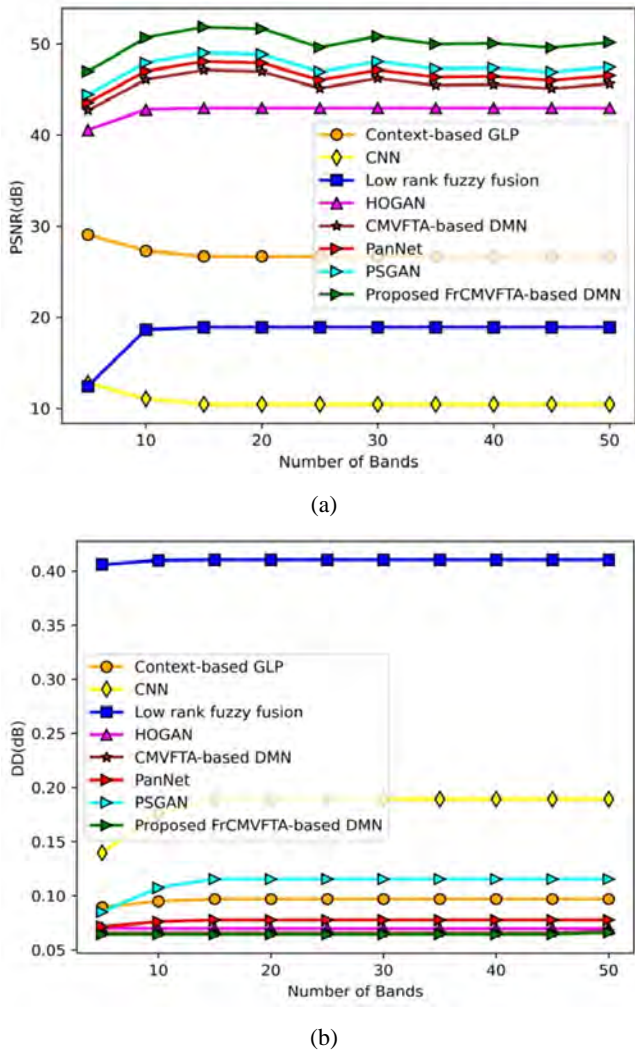


**Figure 4** Comparative analysis of developed FrCMVFTA-based DMN using Indian Pines with a number of bands, (a) PSNR (b) DD (c) SSIM (d) CC (see online version for colours)

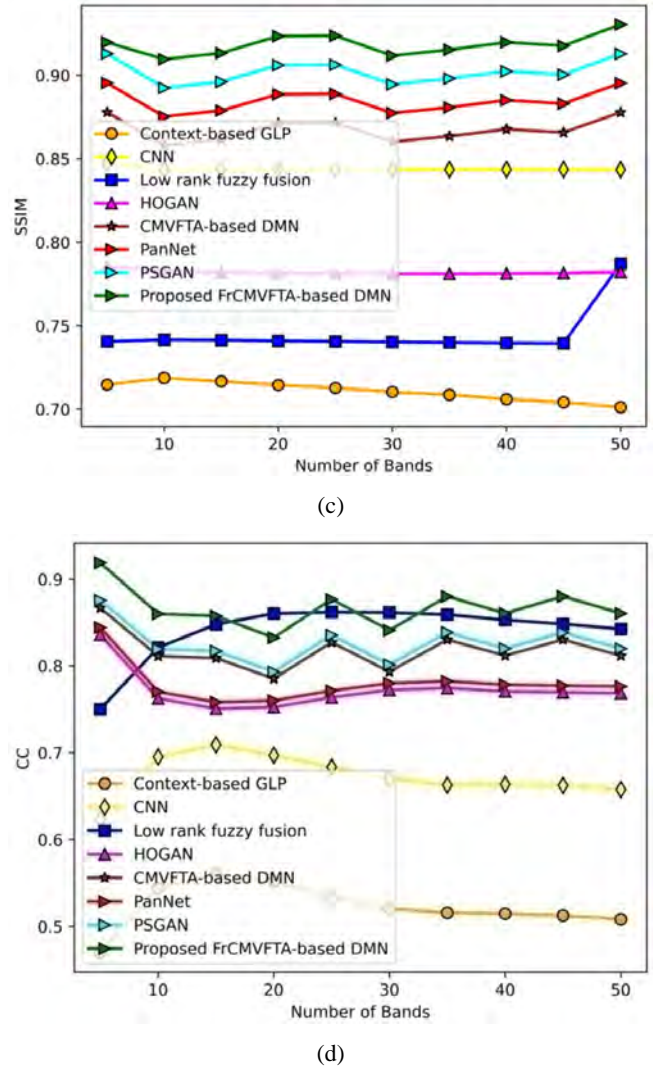


**Figure 5** Comparative analysis of introduced FrCMVFTA-based DMN using Indian Pines with different neta value, (a) PSNR (b) DD (c) SSIM (d) CC (see online version for colours)

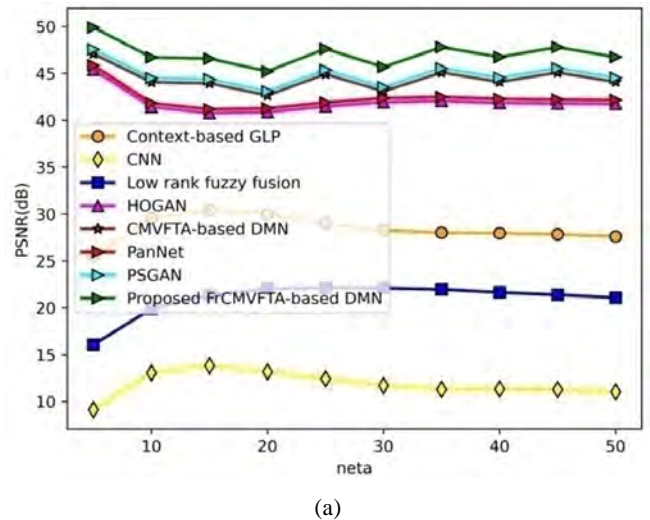
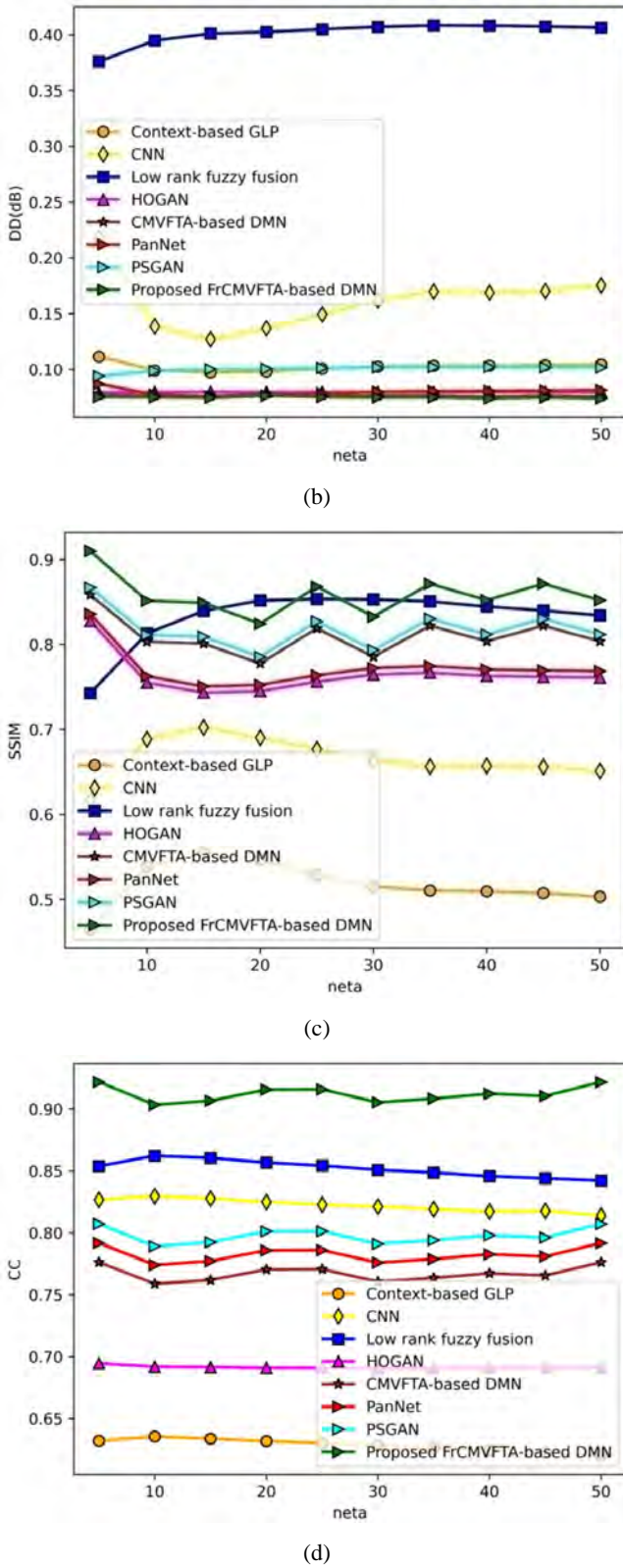


**Figure 5** Comparative analysis of introduced FrCMVF<sub>T</sub>A-based DMN using Indian Pines with different neta value, (a) PSNR (b) DD (c) SSIM (d) CC (continued) (see online version for colours)



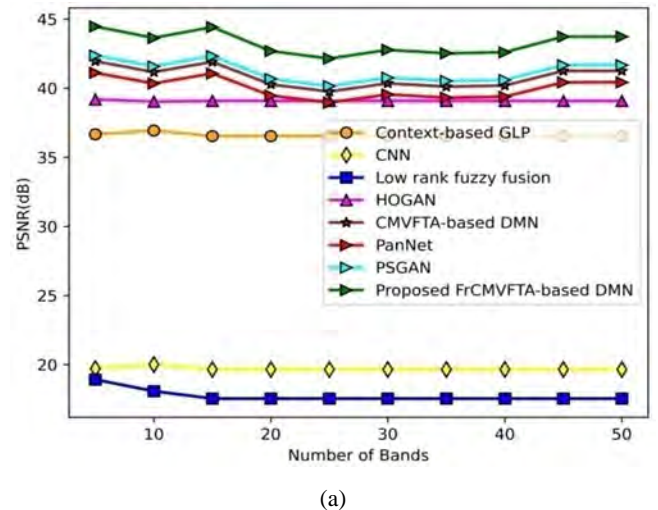
### 6.5.2 Comparative analysis using Pavia

The analysis of developed FrCMVF<sub>T</sub>A-based DMN based on Pavia data through shifting number of bands and neta is plotted in this section.

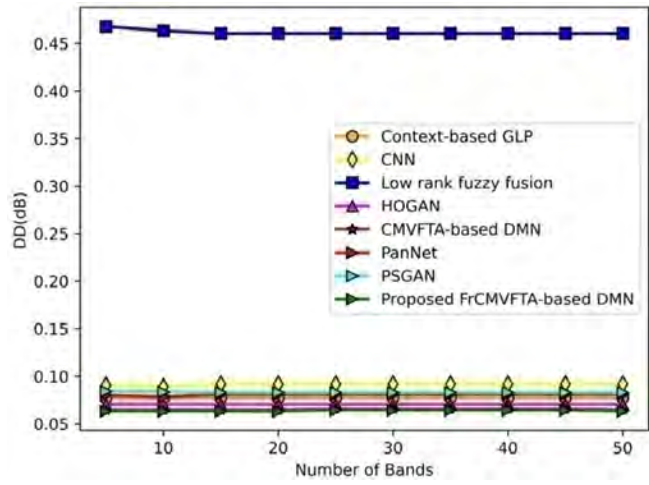
#### 1 Analysis by changing the number of bands

Figure 6 displays the study of a DMN built on the FrCMVF<sub>T</sub>A for performance measures with various band counts. Figure 6(a) shows the results of the PSNR analysis of the newly created FrCMVF<sub>T</sub>A-based DMN. The created FrCMVF<sub>T</sub>A-based DMN has a PSNR of 42.688 dB in 20 bands, compared to 36.538 dB for context-based GLP, 19.653 dB for CNN, 17.544 dB for low rank fuzzy fusion, 39.079 dB for HOGAN, 40.272 dB for PanNet, 39.466 dB for PSGAN, and 40.674 dB for CMVF<sub>T</sub>A-based DMN. The generated FrCMVF<sub>T</sub>A-based DMN for DD is evaluated in Figure 6(b). A developed FrCMVF<sub>T</sub>A-based DMN's DD in 40 bands is 0.064 dB, compared to 0.077 dB, 0.092 dB, 0.460 dB, 0.070 dB, 0.066 dB, 0.081 dB, and 0.083 dB for context-based GLPs, CNNs, low rank fuzzy fusions, HOGANs, PanNets, and PSGANs. Figure 6(c) shows the new FrCMVF<sub>T</sub>A-based DMN for SSIM analysis. The SSIM of the newly developed FrCMVF<sub>T</sub>A-based DMN in the 20 bands is 0.924 dB, compared to 0.714 dB, 0.731 dB, 0.781 dB, 0.741 dB, 0.781 dB, 0.871 dB, 0.889 dB, and 0.906 dB for CNN, CNN-based GLP, low rank fuzzy fusion, HOGAN, PanNet, and CMVF<sub>T</sub>A-based DMN. Figure 6(d) shows the analysis of the recently introduced FrCMVF<sub>T</sub>A-based DMN for CC. The developed FrCMVF<sub>T</sub>A-based DMN's CC in 20 bands is 0.914 dB, compared to 0.707 dB, 0.835 dB, 0.733 dB, 0.773 dB, 0.862 dB, 0.880 dB, and 0.897 dB for context-based GLP, CNN, low rank fuzzy fusion, HOGAN, PanNet, and PSGAN, and CMVF<sub>T</sub>A-based DMN, respectively.

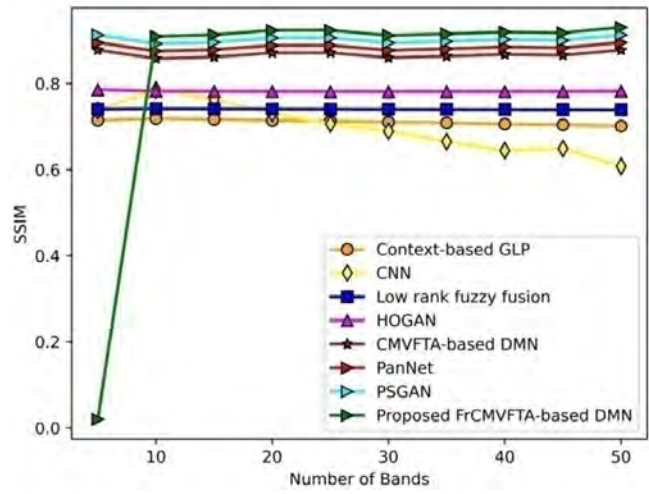
**Figure 6** Comparative analysis of developed FrCMVF<sub>T</sub>A-based DMN using Pavia with number of bands, (a) PSNR (b) DD (c) SSIM (d) CC (see online version for colours)



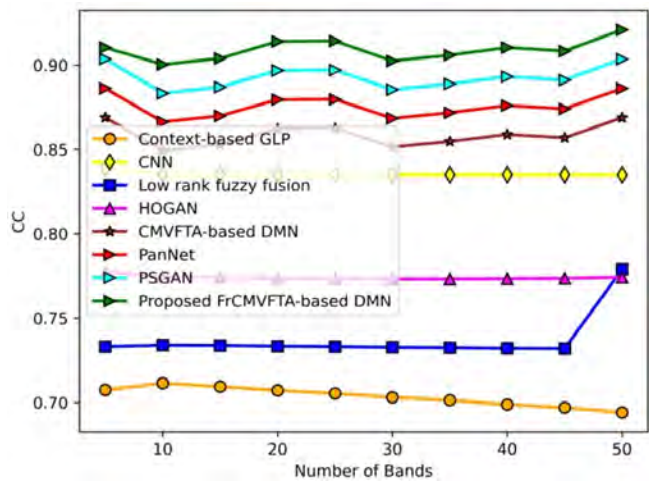
**Figure 6** Comparative analysis of developed FrCMVFTA-based DMN using Pavia with number of bands, (a) PSNR (b) DD (c) SSIM (d) CC (continued) (see online version for colours)



(b)

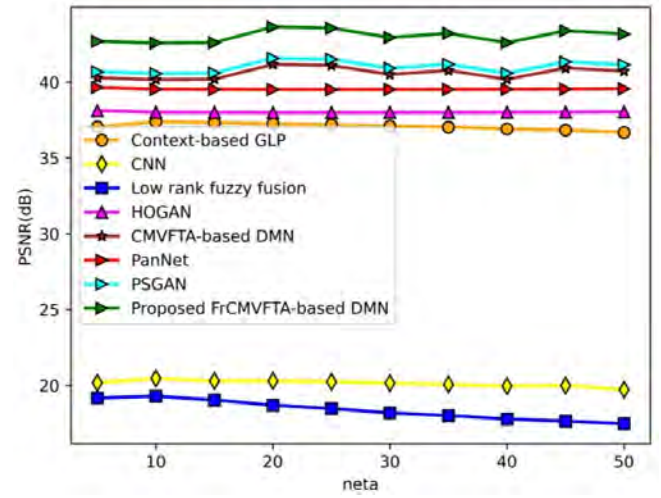


(c)

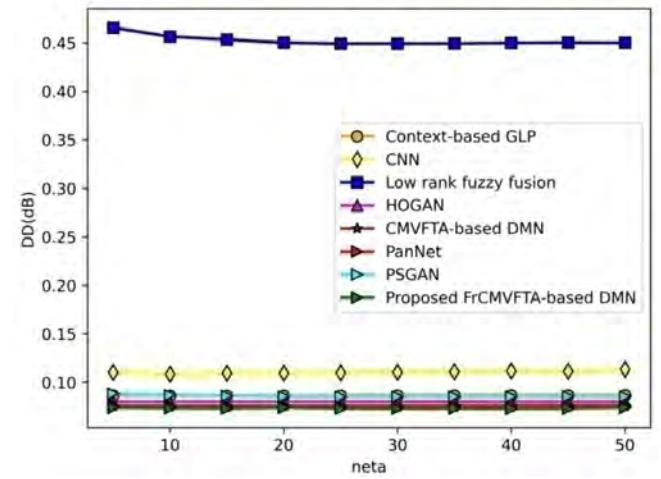


(d)

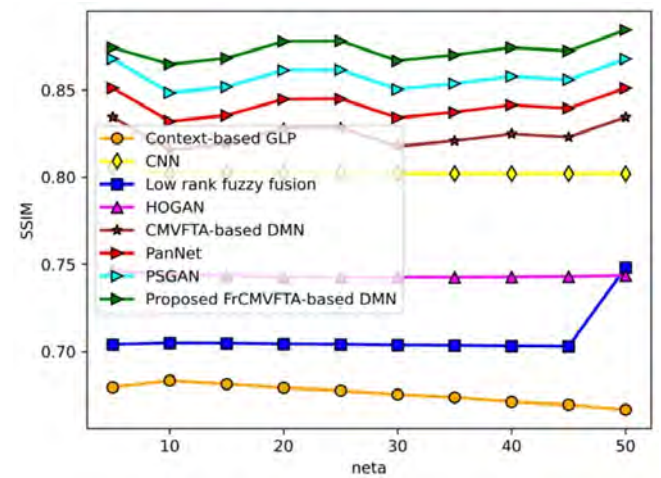
**Figure 7** Comparative analysis of introduced FrCMVFTA-based DMN using Pavia with different neta value, (a) PSNR (b) DD (c) SSIM (d) CC (see online version for colours)



(a)

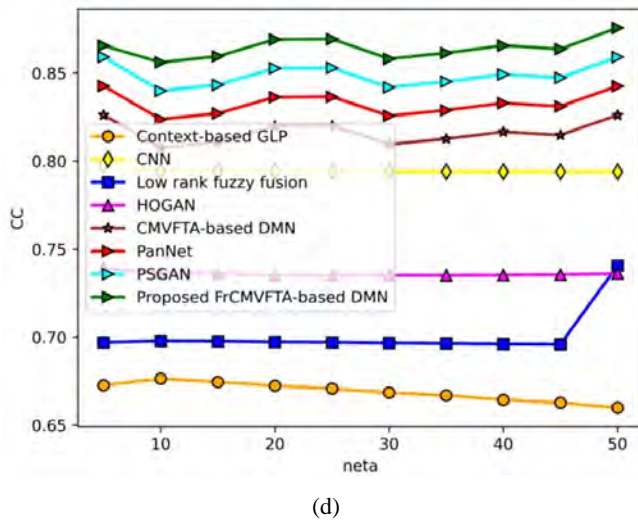


(b)



(c)

**Figure 7** Comparative analysis of introduced FrCMVFITA-based DMN using Pavia with different neta value, (a) PSNR (b) DD (c) SSIM (d) CC (continue) (see online version for colours)



## 2 Analysis by shifting neta value

Figure 7 displays a comparison of the developed FrCMVFITA-based DMN after modifying the neta value with various metrics. Figure 7(a) shows the analysis of the recently implemented FrCMVFITA-based DMN for PSNR. When the neta value is 20, the PSNR of the produced FrCMVFITA-based DMN is 43.635 dB, the PSNR of the context-

based GLP is 37.252 dB, the PSNR of the CNN is 20.300 dB, the PSNR of the low rank fuzzy fusion is 18.703 dB, the PSNR of the HOGAN is 37.997 dB, the PSNR of the PanNet is 41.165 dB, the PSNR of the PSGAN's is 39.517 dB, and PSNR of the CMVFITA-based DMN is 41.577 dB. The analysis of the developed FrCMVFITA-based DMN for DD is shown in Figure 7(b). When neta is 40, the DD of the produced FrCMVFITA-based DMN is 0.073 dB, the DD of the context-based GLP is 0.087 dB, the DD of CNN is 0.112 dB, the DD of the low rank fuzzy fusion is 0.450 dB, the DD of HOGAN is 0.080 dB, the DD of PanNet is 0.074 dB, the DD of PSGAN is 0.076, and CMVFITA-based DMN's DD is 0.085dB. Figure 7(c) shows the analysis of the recently created FrCMVFITA-based DMN for SSIM. The developed FrCMVFITA-based DMN's SSIM is 0.878 dB at a neta value of 20, compared to 0.679 dB for the context-based GLP, 0.802 dB for CNN, 0.704 dB for low rank fuzzy fusion, 0.743 dB for HOGAN, 0.828 dB for PanNet, 0.845 dB for PSGAN, and 0.861 dB for CMVFITA-based DMN. Figure 7(d) presents the analysis of the recently implemented FrCMVFITA-based DMN for CC. The CC of the created FrCMVFITA-based DMN is 0.869 dB when neta is 20, compared to 0.794 dB for CNN, 0.697 dB for Low rank fuzzy fusion, 0.735 dB for HOGAN, 0.820 dB for PanNet, 0.836 dB for PSGAN, and 0.853 dB for the CMVFITA-based DMN.

**Table 1** Comparative discussion

Variation	Metrics	Context-based GLP	CNN	Low rank fuzzy fusion	HOGAN	CMVFITA-based DMN	PanNet	PSGAN	Developed FrCMVFITA-based DMN
<i>Dataset</i>		<i>Indian pines</i>							
Number of bands	DD (dB)	0.089	0.140	0.406	0.070	0.066	0.071	0.085	0.064
	PSNR (dB)	26.667	10.453	18.892	42.952	47.130	48.072	49.034	51.843
	SSIM (dB)	0.701	0.844	0.787	0.782	0.878	0.895	0.913	0.930
	CC (dB)	0.470	0.623	0.750	0.836	0.867	0.844	0.876	0.919
Neta	DD (dB)	0.097	0.127	0.401	0.080	0.076	0.076	0.100	0.075
	PSNR (dB)	25.523	9.138	16.052	45.404	47.088	45.859	47.559	49.913
	SSIM (dB)	0.465	0.617	0.743	0.828	0.858	0.836	0.867	0.910
	CC (dB)	0.620	0.814	0.842	0.692	0.776	0.792	0.807	0.922
<i>Dataset</i>		<i>Pavia</i>							
Number of bands	DD (dB)	0.077	0.092	0.460	0.070	0.065	0.081	0.083	0.063
	PSNR (dB)	36.667	19.724	18.921	39.184	41.952	41.113	42.372	44.469
	SSIM (dB)	0.701	0.608	0.739	0.782	0.878	0.895	0.913	0.930
	CC (dB)	0.694	0.835	0.779	0.774	0.869	0.886	0.904	0.921
Neta	DD (dB)	0.086	0.108	0.457	0.080	0.075	0.076	0.087	0.073
	PSNR (dB)	37.252	20.300	18.703	37.997	41.165	39.517	41.577	43.635
	SSIM (dB)	0.679	0.802	0.704	0.743	0.828	0.845	0.861	0.878
	CC (dB)	0.660	0.794	0.741	0.736	0.826	0.843	0.859	0.876

## 6.6 Comparative discussion

Table 1 shows a comparison of developed FrCMVFTA-based DMNs that were based on various datasets for DD and PSNR measures. In 50 bands, the developed FrCMVFTA-based DMN's PSNR is 51.843 dB, compared to 26.667 dB for context-based GLP, 10.452 dB for CNN, 18.892 dB for low rank fuzzy fusion, 42.952 dB for HOGAN, 47.130 dB for CMVFTA-based DMN, 48.072 dB for PanNet, and 49.034 dB for PSGAN using data from Indian pines. Based on the weighted nonlinear regression model that is being used, the PSNR of the developed FrCMVFTA-based DMN is much improved. For 50 bands, the DD of existing approaches and the FrCMVFTA-based DMN that was developed using data from pavia 0.077 dB, 0.092 dB, 0.460 dB, 0.070 dB, 0.065 dB, 0.081 dB, 0.083 dB, and 0.063 dB. The use of the hybrid optimisation strategy reduces the DD of the developed pan-sharpening technique.

## 7 Conclusions

This research presents an effective pan-sharpening solution based on the FrCMVFTA-based DMN. The pan-sharpening procedure takes into account the images, such as HR-MSI and LR-MSI. The weighted nonlinear regression model's output image is provided to DMN, whose priors are trained using the residual learning model. The DMN is also trained using a developed optimisation method known as FrCMVFTA. As a result, the FAT, CMVO, and FC methods were combined to create the newly designed FrCMVFTA. Here, the CMVO algorithm was used to solve engineering problems, but the FC model experienced less information loss. The FrCMVFTA optimisation model that was developed as a result is an efficient solution for deep learning technique training. The performance of pan sharpening is improved by DMN's greatly reduced computational cost and computational complexity. The PSNR and DD measurements are also employed to evaluate the efficiency of the proposed pan sharpening method. As a result, the FrCMVFTA-based DMN that was introduced performed better, with a DD of 0.063 dB and a PSNR of 51.843dB. The developed pan sharpening approach can also be expanded by taking into account more significant datasets and hybrid optimisation algorithms.

## References

- Bhanot, A. (2021) 'The role of confidence and trust in the ability to understand the effect of social-media marketing on brand loyalty and brand equity', *Academy of Management Journal*, Vol. 64, No. 1.
- Aiazzi, B., Alparone, L., Baronti, S., Carla, R., Garzelli, A. and Santurri, L. (2016) 'Sensitivity of pansharpening methods to temporal and instrumental changes between multispectral and panchromatic data sets', *IEEE Transactions on Geoscience and Remote Sensing*, September, Vol. 55, No. 1, pp.308–319.
- Aiazzi, B., Baronti, S. and Selva, M. (2007) 'Improving component substitution pansharpening through multivariate regression of MS + Pan data', *IEEE Transactions on Geoscience and Remote Sensing*, September, Vol. 45, No. 10, pp.3230–3239.
- Benmessahel, I., Xie, K. and Chellal, M. (2020) 'A new competitive multiverse optimization technique for solving single-objective and multiobjective problems', *Engineering Reports*, March, Vol. 2, No. 3, p.e12124.
- Bhaladhare, P.R. and Jinwala, D.C. (2014) 'A clustering approach for the l-diversity model in privacy preserving data mining using fractional calculus-bacterial', *Advances in Computer Engineering*, Vol. 2014, No. 1, DOI: 10.1155/2014/396529.
- Bovolo, F., Bruzzone, L., Capobianco, L., Garzelli, A., Marchesi, S. and Nencini, F. (2009) 'Analysis of the effects of pansharpening in change detection on VHR images', *IEEE Geoscience and Remote Sensing Letters*, September, Vol. 7, No. 1, pp.53–57.
- Cai, J. and Huang, B. (2020) 'Super-resolution-guided progressive pansharpening based on a deep convolutional neural network', *IEEE Transactions on Geoscience and Remote Sensing*, August, Vol. 59, No. 6, pp.5206–5220.
- Dian, R., Li, S., Fang, L. and Wei, Q. (2019) 'Multispectral and hyperspectral image fusion with spatial-spectral sparse representation', *Information Fusion*, September, Vol. 49, pp.262–270.
- Dian, R., Li, S., Guo, A. and Fang, L. (2018) 'Deep hyperspectral image sharpening', *IEEE Transactions on Neural Networks and Learning Systems*, Vol. 29, No. 11, pp.5345–5355.
- He, L., Zhu, J., Li, J., Meng, D., Chanussot, J. and Plaza, A. (2020) 'Spectral-fidelity convolutional neural networks for hyperspectral pansharpening', *IEEE Journal of Selected Topics in Applied Earth Observations and Remote Sensing*, September, Vol.13, pp.5898–5914.
- He, Y., Yap, K.H., Chen, L. and Chau, L.P. (2007) 'A nonlinear least square technique for simultaneous image registration and super-resolution', *IEEE Transactions on Image Processing*, October, Vol. 16, No. 11, pp.2830–2841.
- Hou, L. and Zhang, X. (2016) 'Pansharpening image fusion using cross-channel correlation: a framelet-based approach', *Journal of Mathematical Imaging and Vision*, May, Vol. 55, No. 1, pp.36–49.
- Indian Pines and Pavia Centre and University Data (2022) Hyperspectral Remote Sensing Scenes database [online] [http://www.ehu.es/ccwintco/index.php/Hyperspectral\\_Remote\\_Sensing\\_Scenes](http://www.ehu.es/ccwintco/index.php/Hyperspectral_Remote_Sensing_Scenes) (accessed February 2022).
- Kwon, H. and Tai, Y.W. (2015) 'RGB-guided hyperspectral image upsampling', *Proceedings of the IEEE International Conference on Computer Vision*, pp.307–315.
- Li, Q.Q., He, Z.C. and Li, E. (2020) 'The feedback artificial tree (FAT) algorithm', *Soft Computing*, February, Vol. 24, pp.13413–13440.
- Li, Y., Xie, W. and Li, H. (2017) 'Hyperspectral image reconstruction by deep convolutional neural network for classification', *Pattern Recognition*, March, Vol. 63, pp.371–383.
- Lin, C., Chen, S.Y., Chen, C.C. and Tai, C.H. (2018) 'Detecting newly grown tree leaves from unmanned-aerial-vehicle images using hyperspectral target detection techniques', *ISPRS Journal of Photogrammetry and Remote Sensing*, August, Vol. 142, pp.174–189.

- Liu, X., Wang, Y. and Liu, Q. (2018a) 'Psgan: a generative adversarial network for remote sensing image pan-sharpening', *2018 25th IEEE International Conference on Image Processing (ICIP)*, pp.873–877, doi: 10.1109/ICIP.2018.8451049.
- Liu, Y., Chen, X., Wang, Z., Wang, Z.J., Ward, R.K. and Wang, X. (2018b) 'Deep learning for pixel-level image fusion: recent advances and future prospects', *Information Fusion*, Vol. 42, pp.158–173.
- Luo, S., Zhou, S., Feng, Y. and Xie, J. (2020) 'Pansharpening via unsupervised convolutional neural networks', *IEEE Journal of Selected Topics in Applied Earth Observations and Remote Sensing*, July, Vol. 13, pp.4295–4310.
- Lv, X., Ming, D., Chen, Y. and Wang, M. (2019) 'Very high resolution remote sensing image classification with SEEDS-CNN and scale effect analysis for superpixel CNN classification', *International Journal of Remote Sensing*, January, Vol. 40, No. 2, pp.506–531.
- Ma, J., Yu, W., Chen, C., Liang, P., Guo, X. and Jiang, J. (2020) 'Pan-GAN: an unsupervised pan-sharpening method for remote sensing image fusion', *Information Fusion*, October, Vol. 62, pp.110–120.
- Masi, G., Cozzolino, D., Verdoliva, L. and Scarpa, G. (2016) 'Pansharpening by convolutional neural networks', *Remote Sensing*, July, Vol. 8, No. 7, p.594.
- Qian, R., Tan, R.T., Yang, W., Su, J. and Liu, J. (2018) 'Attentive generative adversarial network for raindrop removal from a single image', *Proceedings of the IEEE Conference on Computer Vision and Pattern Recognition*, pp.2482–2491.
- Shao, Z., Fu, H., Li, D., Altan, O. and Cheng, T. (2019) 'Remote sensing monitoring of multi-scale watersheds impermeability for urban hydrological evaluation', *Remote Sensing of Environment*, October, Vol. 232, p.111338.
- Simone, G., Farina, A., Morabito, F.C., Serpico, S.B. and Bruzzone, L. (2002) 'Image fusion techniques for remote sensing applications', *Information Fusion*, March, Vol. 3, No. 1, pp.3–15.
- Sun, W., Su, F. and Wang, L. (2018) 'Improving deep neural networks with multi-layer maxout networks and a novel initialization method', *Neurocomputing*, February, Vol. 278, pp.34–40.
- Vivone, G., Marano, S. and Chanussot, J. (2020) 'Pansharpening: context-based generalized Laplacian pyramids by robust regression', *IEEE Transactions on Geoscience and Remote Sensing*, March, Vol. 58, No. 9, pp.6152–6167.
- Wang, J., Huang, B., Zhang, H.K. and Ma, P. (2019) 'Sentinel-2A image fusion using a machine learning approach', *IEEE Transactions on Geoscience and Remote Sensing*, August, Vol. 57, No. 12, pp.9589–9601.
- Wang, J., Shao, Z., Huang, X., Lu, T. and Zhang, R. (2021) 'A dual-path fusion network for pan-sharpening', *IEEE Transactions on Geoscience and Remote Sensing*, June, Vol. 60.
- Wu, C.X., Liao, M.H., Karatas, M., Chen, S.Y. and Zheng, Y.J. (2020) 'Real-time neural network scheduling of emergency medical mask production during COVID-19', *Applied Soft Computing*, Vol. 97, p.106790.
- Xie, W., Cui, Y., Li, Y., Lei, J., Du, Q. and Li, J. (2020) 'HPGAN: Hyperspectral pansharpening using 3-D generative adversarial networks', *IEEE Transactions on Geoscience and Remote Sensing*, May, Vol.59, No. 1, pp.463–477.
- Yang, J., Fu, X., Hu, Y., Huang, Y., Ding, X. and Paisley, J. (2017a) 'PanNet: a deep network architecture for pan-sharpening', *Proceedings of the IEEE International Conference on Computer Vision*, pp.5449–5457.
- Yang, J., Fu, X., Hu, Y., Huang, Y., Ding, X. and Paisley, J. (2017b) 'PanNet: a deep network architecture for pan-sharpening', *2017 IEEE International Conference on Computer Vision (ICCV)*, doi:10.1109/iccv.2017.193.
- Yang, Y., Wan, C., Huang, S., Lu, H. and Wan, W. (2020) 'Pansharpening based on low-rank fuzzy fusion and detail supplement', *IEEE Journal of Selected Topics in Applied Earth Observations and Remote Sensing*, September, Vol. 13, pp.5466–5479.
- Yuan, Q., Zhang, Q., Li, J., Shen, H. and Zhang, L. (2018) 'Hyperspectral image denoising employing a spatial-spectral deep residual convolutional neural network', *IEEE Transactions on Geoscience and Remote Sensing*, September Vol. 57, No. 2, pp.1205–1218.
- Zhang, G., Da, Q., Li, S., Sun, J., Wang, W., Hu, Q. and Lu, J. (2022a) 'Adversarial transformation network with adaptive perturbations for generating adversarial examples', *International Journal of Bio-Inspired Computation*, Vol. 20, No. 2, pp.94–103.
- Zhang, N., Wang, F., Chen, X., Zhao, T. and Kang, Q. (2022b) 'Spatial-temporal attention-based seq2seq framework for short-term travel time prediction', *International Journal of Bio-Inspired Computation*, Vol. 20, No. 1, pp.23–37.
- Zheng, Y-J., Gao, C-C., Huang, Y-J., Sheng, W-G. and Wang, Z. (2022) 'Evolutionary ensemble generative adversarial learning for identifying terrorists among high-speed rail passengers', *Expert Systems with Applications*, Vol. 210, p.118430.
- Zhou, X-H., Zhang, M-X., Xu, Z-G., Cai, C-Y., Huang, Y-J. and Zheng, Y-J. (2019) 'Shallow and deep neural network training by water wave optimization', *Swarm and Evolutionary Computation*, Vol. 50, p.100561.